Indian Journal of Engineering & Materials Sciences
Vol. 33, June 2026, pp. 279-286
DOI: 10.56042/ijems.v33i03.25679

Effect of molybdenum-based precursors on the morphological evolution of $MoTe_2$ nanostructures prepared by a one-pot synthesis method

Vinay Kumar Yadav & Mohan Singh Mehata*

Laser Spectroscopy Laboratory, Department of Applied Physics, Delhi Technological University, Bawana Road, Delhi 110042, India

Received: 19 November 2025; accepted: 24 April 2026

In this work, molybdenum ditelluride ($MoTe_2$) nanostructures have been synthesized using a hydrothermal route with different precursors and investigated for their morphological, structural and optical properties. Field-emission scanning electron microscopic images have revealed different morphological growth patterns, including nanorods, agglomerated nanoparticles and stacked sheet/flake-like structures, demonstrating significant influence of precursors and temperature on morphology. High-resolution transmission electron microscopy further confirmed the polycrystalline nature of the synthesized $MoTe_2$ nanostructures. X-ray diffraction patterns have confirmed the existence of 1T and 2H phases of $MoTe_2$, depending on the selection of molybdenum precursors. The average crystallite size, calculated using the Williamson-Hall plot to be 144, 91, 57 and 41 nm for NAMo-1, NAMo-2, NHMo-1 and NHMo-2, samples respectively. The active A_g and B_{2g} modes have been confirmed by Raman spectra and characteristic Mo-Te and Mo-O vibration modes by Fourier-transform infrared spectra, further confirmed the formation of $MoTe_2$ nanostructures. The precursor-dependent morphology has provided insights into the synthesis of phase-tunable nanostructures.

Keywords: Hydrothermal, Molybdenum ditelluride **(**$MoTe_2$), Nanostructures (NSs)

1 Introduction

In recent years, molybdenum ditelluride ($MoTe_2$) has emerged as a prominent member of the transition metal dichalcogenide (TMD) family, which encompasses extensive investigations similar to those of molybdenum diselenide ($MoSe_2$), molybdenum disulfide (MoS_2), tungsten diselenide (WSe_2) and tungsten disulfide (WS_2)[1–7]. These nanostructured materials consist of layered atomic sheets with a transition metal atom sandwiched between two chalcogen atoms. The weak van der Waals forces hold them together, allowing them to exfoliate in two dimensions and imparting them unique anisotropic properties[3,6]. $MoTe_2$ stands out among these because it has a lower bandgap (~ 1 eV for the semiconducting 2H phase) and a higher intrinsic electrical conductivity, which makes it more suitable for the near-infrared spectrum of electronics and optoelectronics devices[8]. Additionally, $MoTe_2$ exhibits a unique advantage under moderate synthesis conditions: it can undergo easy and reversible phase transitions between the semiconducting 2H phase and the metallic 1T phase. Unlike MoS_2 and $MoSe_2$, where such transitions are challenging to achieve, $MoTe_2$ offers greater electronic phase tunability, enabling more versatile device functionality [2]. In addition, $MoTe_2$ has stronger molecule adsorption and better charge transfer capability, which is translated into better catalytic and sensing ability, especially observable in gas sensing and hydrogen evolution reaction applications[9]. These special structural, chemical, and electrical characteristics render $MoTe_2$ an extremely promising material for next-generation optoelectronic, nanoelectronics, and energy conversion devices [9,10].

Hydrothermal synthesis has proven to be a robust method for the synthesis of $MoTe_2$ nanostructures with high crystallinity, phase purity, and morphological control[11–13]. The choice of synthesis route and precursor determines the nucleation, growth, and morphology of $MoTe_2$, which in turn determines properties crucial for specific applications. For example, precursor variation of the type of sodium or ammonium molybdate, tellurium/sulphur precursor, the growth temperature, and the reaction conditions affect whether nanoparticles/quantum dots, nanorods, agglomerated particles, or nanosheets are synthesized, as well as their phase composition[11–17]. Identification of these morphological differences by systematic investigation illuminates the growth kinetics, the phase formation mechanism, enabling intentional growth of $MoTe_2$ structures for maximum

*Corresponding author (E-mail: msmehata@gmail.com)

catalytic activity, surface reactivity, and electronic conductivity [18].

This study investigates the effects of molybdenum-based precursors and growth temperature on the morphology, phase and crystallinity of $MoTe_2$ nanostructures, aiming to elucidate the underlying growth mechanisms and enable controlled synthesis for further electronics, optoelectronics, catalysis and energy conversion applications [10–14].

2 Materials and Methods

2.1 Materials and synthesis

All chemicals of analytical reagent (AR) spectroscopic grade were used without any further purification. Tellurium powder (Te) (99.2%) from SRL, sodium borohydride ($NaBH_4$) (95%) from CDH, and sodium molybdate ($Na_2MoO_4.2H_2O$) and ammonium molybdate ($(NH_4)_6Mo_7O_{24}.4H_2O$) from Sigma-Aldrich were procured for the synthesis of $MoTe_2$ nanostructures. The deionized (DI) ultrapure water with a resistivity of 18.2 MΩ-cm was used in synthesis.

$MoTe_2$ nanostructures were synthesized by the hydrothermal route. First, Te powder (2 mM) and $NaBH_4$ (3 mM) were dissolved in 20 mL DI water. After 1 hour of continuous stirring, a clear Te solution was obtained. In the meantime, $Na_2MoO_4.2H_2O$ (1 mM) was dispersed in 50 mL DI water to obtain a homogeneous solution. Then, the Te solution was slowly added to the above homogeneous solution and stirred for one hour. After the mixture was transferred to a Teflon-lined stainless-steel autoclave, the autoclave was placed inside an oven at 180 ± 5 ℃ (NAMo-1) and 200 ± 5 ℃ (NAMo-2) for 48 hours (though the exact temperature inside the autoclave could not be recorded in the used setup). The final product was washed with an excess of DI water and ethanol and then vacuum-dried at 60℃ for several hours, and used for further characterization. For the preparation of ammonium molybdate precursor, similar steps were used as we mentioned above, only ammonium molybdate was used in place of sodium molybdate and named as (NHMo-1 and NHMo-2). The sample names according the used Mo precursors have been summarized in Table 1.

Table 1 — Samples name with different Mo precursors

Mo precursor	Sample name
Sodium molybdate	NAMo-1
Sodium molybdate	NAMo-2
Ammonium molybdate	NHMo-1
Ammonium molybdate	NHMo-2

2.2 Materials characterization

Morphology of $MoTe_2$ nanostructures were examined using field emission scanning electron microscope (FE-SEM) using a Zeiss Sigma-360 operated at 10 kV, and high-resolution transmission electron microscopy (HR-TEM) with a JEOL JEM-F200 operated at an accelerating voltage of 200 kV, providing insights into the size, shape, and crystal structure of the MoTe2 nanostructures. The structural and phase formation of MoTe2 nanostructures were examined with a PANalytical Empyrean X-ray diffractometer (XRD) with a wavelength of 1.54 Å of Cu-Kα source. The Fourier transform infrared (FT-IR) spectra of the synthesized MoTe2 nanostructures were acquired using a Nicolet Summit X FTIR spectrometer (Thermo Scientific), covering a spectral range from 400 to 4000 cm^{-1}. To study the molecular fingerprints of MoTe2 nanostructures, a micro-Raman spectrometer equipped with a 532 nm laser source and a 20x objective lens was used.

3 Results and Discussion

3.1 Field emission scanning electron microscopy

The morphological evolution of $MoTe_2$ nano structures obtained using sodium molybdate as the Mo precursor at two different growth temperatures is illustrated in Fig. 1(a-d). The FE-SEM images of the sample NAMo-1, as shown in Fig. 1(a, b), show that the synthesized material predominantly consists of small, irregularly shaped particles that tend to aggregate into bulk-like structures through particle coalescence. The individual particles exhibit sizes in the nano range (~74 nm) and display a tendency toward agglomeration, forming densely packed assemblies with an aspect ratio of approximately 1.3[19].

The FE-SEM images of the sample NAMo-2, as shown in Fig. 1(c, d), exhibits a clear morphological transition and the development of well-faceted nanorod structures alongside residuals. This morphological transition due to temperature may favor anisotropic growth of crystals in one-dimensional nanostructures over isotropic growth of particles. The nanorods, with an average length of 347 nm, have greater aspect ratios (length/diameter) [20] around 5.8, and more uniform sizes than the sample formed at lower temperatures. The presence of both particles and nanorods at higher growth temperature

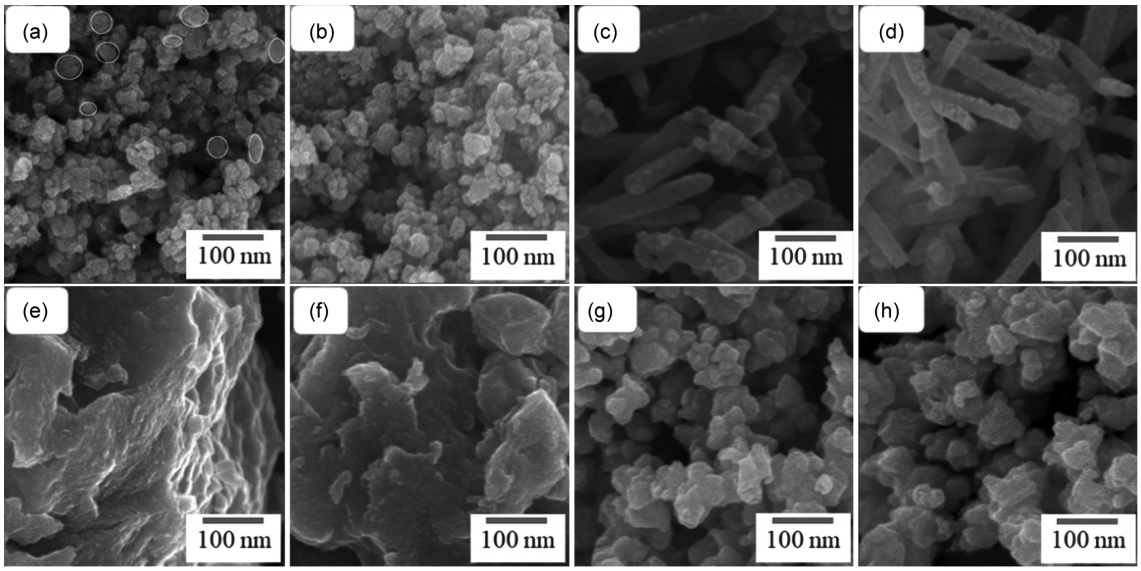


Fig. 1 —FE-SEM images of (synthesized $MoTe_2$ structures) (a, b) samples NAMo-1, (c, d) NAMo-2, (e, f) NHMo-1 and (g, h) NHMo-2 samples.

Table 2 — Comparison of $MoTe_2$ having different morphologies with different precursors.

Precursor Used	Morphology	Method & Growth Temperature
Sodium molybdate dihydrate, tellurium powder, sodium borohydride	Nanosheets	Hydrothermal, 160- 240 °C[12]
Sodium molybdate dihydrate, tellurium powder, hydrazine hydrate	Nanoparticles	Hydrothermal, 200 °C [18]
Tantalum sulfide, ammonium molybdate, thiourea, selenium Powder, tellurium powder, hydrazine hydrate, NMP.	Nanosheets	Hydrothermal, 180– 200 °C[21]
Sodium molybdate dihydrate, Sodium Borohydride, Tellurium Powder.	Quantum dots	Hydrothermal, 200 °C[22]
Ammonium heptamolybdate tetrahydrate, dopamine hydrochloride powder	Nanoflowers	Chelation, peroxidation, and tellurization, 600-700 °C[23]
Ammonium molybdate, titanium aluminium carbide, hydrofluoric acid, sulfuric acid, and isopropyl alcohol, tellurium dioxide, hydrazine hydrate	Nanosheets	Hydrothermal, 200 °C[24]
Sodium molybdate dihydrate, tellurium metal powder, sodium borohydride	Nanotubes	Hydrothermal, 200 °C[25]
Oleyl amine, tellurium, trioctylphosphine, hexacarbonyl molybdenum, and molybdenum pentachloride	Nanosheets	Colloidal Method, 320 °C[26]
Tellurium dioxide, ammonium molybdate, selenium dioxide	Nanosheets	One Pot Reaction, 80 °C[10]
Tellurium powders, sodium molybdate dihydrate, sodium borohydride	Nanoparticles	Hydrothermal, 200 °C[9]

suggests a transition regime of growth leading to bimodal morphologies.

The morphology of $MoTe_2$ synthesized at a lower temperature, NHMo-1, as shown in Fig. 1(e, f), comprises a typical stacked flake/sheet-like morphology. The FESEM images of NHMo-2, as shown in Fig. 1(g, h), reveal a considerable morphological change from the stacked sheet structures of NHMo-1, which are broken up and reorganized into separate particulate structures. A comparison of the formation of different morphologies with different precursors is given in Table 2.

3.2 High-resolution transmission electron microscopy (HR-TEM)

The HR-TEM images of the sample NAMo-1, as shown in Fig. 2(a), show that the particles are closely packed, and the lattice fringes orientation in multiple directions demonstrates the polycrystalline nature of the sample. The calculated d-spacing, as shown in the inset of Fig. 2(a), is approximately 2.3 Å. The selected area electron diffraction (SAED) shown in Fig. 2(b) exhibits a pattern with diffraction spots forming a circle, indicating that the $MoTe_2$ made at lower temperatures is polycrystalline. The image of NAMo-2 shown in Fig. 2(c) demonstrates that the morphology changed into rod-like shapes when the growth temperature was increased. The clear lattice fringes were observed, and the estimated d-spacing was about 3.2 Å, as shown in the inset Fig. 2(c). The diffraction rings in the SAED pattern, as shown in

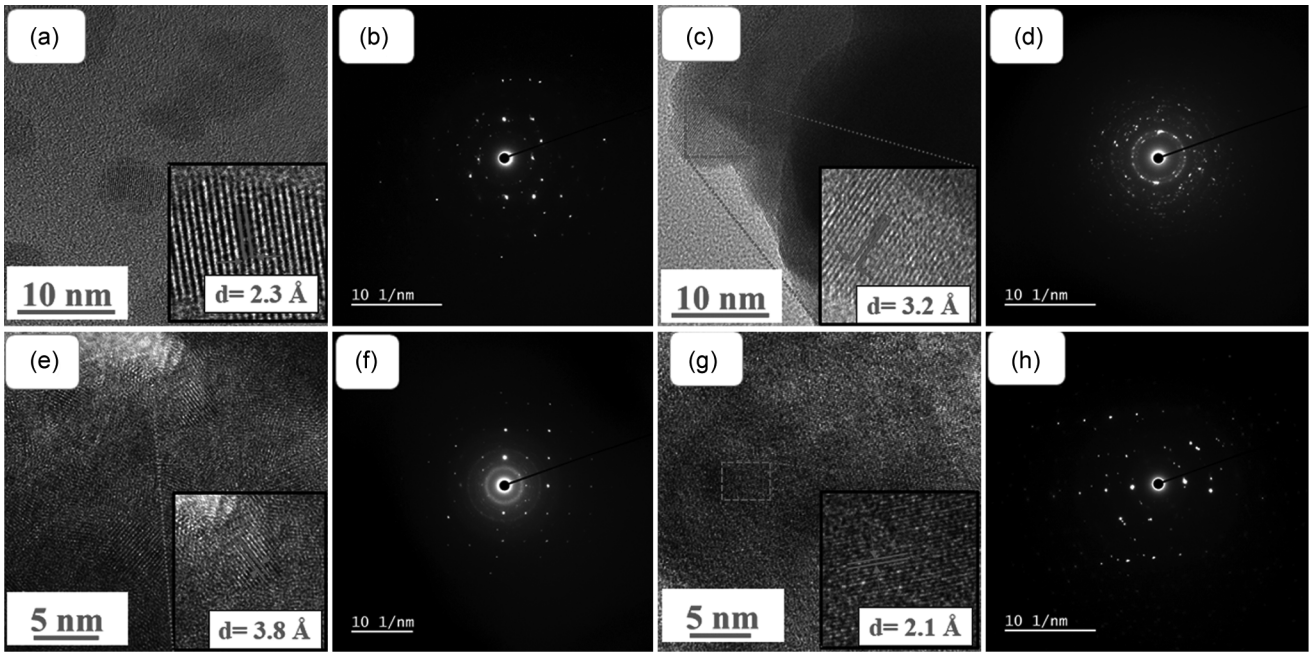


Fig. 2 — HR-TEM images and SAED patterns of samples (a, b) NAMo-1, (c, d) NAMo-2, (e, f) NHMo-1 and (g, h) NHMo-2.

Table 3 — Calculated d-spacing and the corresponding planes.

Sample	d-spacing (Å)	hkl
NAMo-1	3.2	(200)
NAMo-2	2.3	(210)
NHMo-1	3.8	($\bar{1}$03)
NHMo-2	2.1	(106)

Fig. 2(d), demonstrate that the more crystalline growth occurs at higher temperatures.

The image of the NHMo-1 shows a stacked sheet structure, as shown in Fig. 2(e), along with fringe patterns. The SAED pattern shown in Fig. 2(f) demonstrates that the sample has more crystallinity than the NA precursor-derived sample, as diffraction rings are better observable. As the temperature increases, (NHMo-2), the layered sheets break down into nanoparticles, which adhere to one another, as illustrated in Fig. 2(g). The SAED pattern shown in Fig. 2(h) exhibits diffraction spots forming a circle, which demonstrates the polycrystalline nature. The calculated d-spacing values were about 3.8 Å for the layered sheets and 2.1 Å for the agglomerated particles shown in the inset of Fig. 2(e, g). The calculated d spacing and their corresponding planes are summarized in Table 3.

3.3 X-ray diffraction (XRD) patterns

XRD analysis was performed to investigate the crystallographic structure and phase composition of the synthesized $MoTe_2$ samples. The 2θ peaks of NAMo-1(grown at lower temperature) were observed at 23.02°, 27.55°, 38.24°, 40.40°, 43.33°, 49.66°, 56. 89°, 62.81° and 63.78° corresponding Miller indices of ($\bar{1}$03), (200), (212), ($\bar{1}$06), ($\bar{1}$15), ($\bar{2}$15), (122), (222) and ($\bar{2}$23), as illustrated in Fig. 3(a), are well matched with the standard JCPDS file No. (71-257). For NAMo-2 (grown at higher temperature), additional peaks arose, and peaks became more intense and broader, which shows more crystallinity in comparison to grown at lower temperature hence confirmed the formation of monoclinic 1T-$MoTe_2$ [10,12,13]. In contrast, for NHMo-1, grown at lower temperature, the 2θ values are 23.02°, 26.07°, 27.62°, 36.94°, 38.33°, 53.54°, 60.61° and 63.83° corresponding to miller indices ($\bar{1}$03), (004), (200), ($\bar{2}$04), (006), (112), (200) and ($\bar{2}$23), as shown in Fig. 3(b). The respective peaks exhibit broadening along with some additional peaks, confirming the formation of mixed-phase (1T and 2H) of $MoTe_2$ [9,27]. At higher temperature, some of the peaks at higher angles diminished, and the pattern matched well with the JCPDS files (00-070-0155) and (71-257). Therefore, the (200) plane at a lower angle is related to the 1T phase and at a higher angle, the (200) plane is related to the 2H phase. The polycrystalline nature of $MoTe_2$ has also been confirmed from SAED patterns.

The average crystallite size was calculated using Scherrer's equation Eq. (1), and Williamson-Hall (W-H) plots (β Cosθ vs. 4 Sinθ) by Eq. (2),

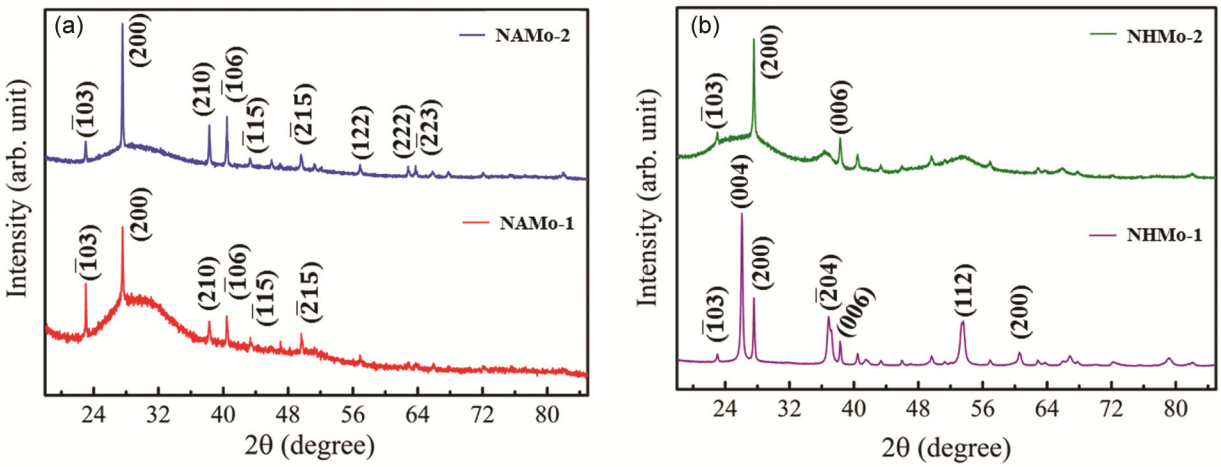


Fig. 3 — XRD patterns of (a) NAMo-1 & NAMo-2 and (b) NHMo-1 & NHMo-2, samples with different $MoTe_2$ structures.

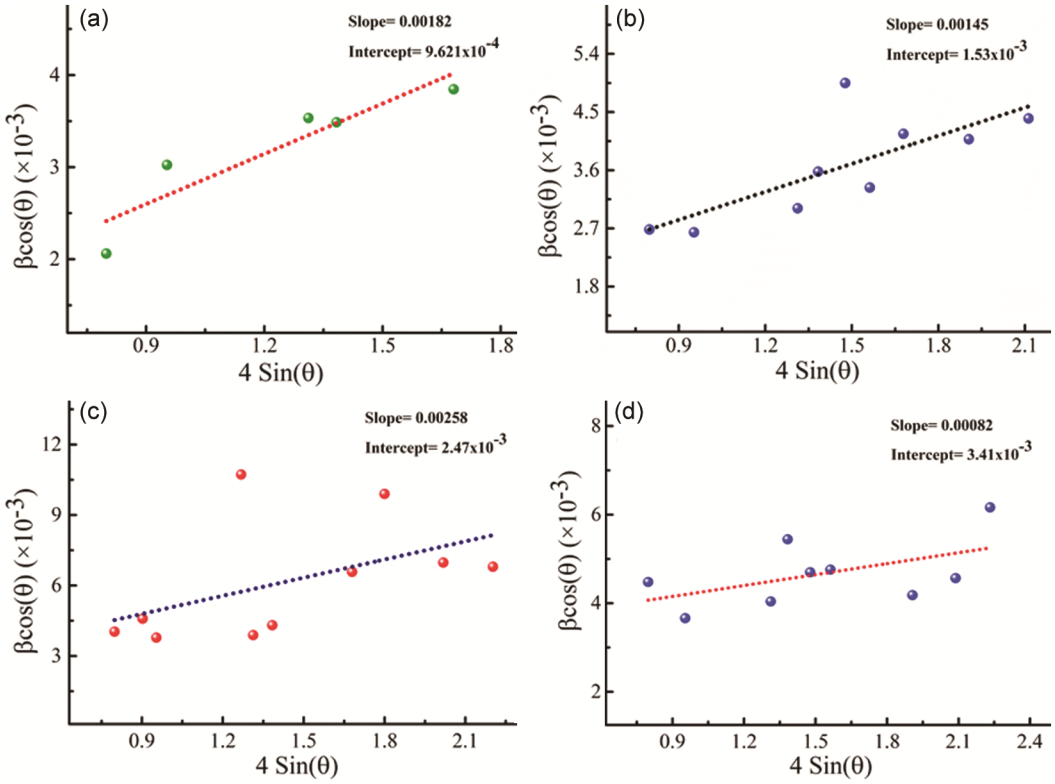


Fig. 4 — W-H plots of $MoTe_2$ structures (a) NAMo-1, (b) NAMo-2, (c) NHMo-1 and (d) NHMo-2.

$$D = k\lambda/\beta\ Cos\theta \quad \ldots (1)$$

$$\beta = \frac{k\lambda}{DCos\theta} + 4\varepsilon tan\theta \quad \ldots (2)$$

where k is the shape factor (k~0.9), λ is the wavelength of X-ray, β is the full width at half maxima, ε is the microstrain, and θ is Bragg's angle. The W-H plots are represented in Fig. 4. The difference in crystallite size calculated from both methods is due to significant microstrain or defects-related broadening in the W-H plot [28,29]. The crystallite size calculated from Scherrer's formula and W-H plot, along with strain, is given in Table 4.

3.4 Raman Spectroscopy

Raman spectroscopy was employed to investigate the vibrational modes of synthesized $MoTe_2$. Two intense Raman peaks at 117 cm^{-1} (^1A_g) and 138 cm^{-1} (^2A_g) were observed for samples synthesized with sodium

molybdate (NAMo-1 and NaMo-2), as shown in Fig. 5(a). The A_g symmetric vibrational modes, arising from different out-of-plane atomic motions of Te and Mo atoms within the layered structure, correspond to those that of typical 1T phase [8,12,30]. As the temperature increases, the intensity and sharpness of the peaks increase, indicating a decrease in defect concentration [12].

The Raman spectra of samples NHMo-1 and NHMo-2, were more complex, as shown in Fig. 5(b). The identified A_g modes emerged at around 120 cm^{-1} (^1A_g) and 139 cm^{-1} (^2A_g), which confirm the existence of the 1T phase [12]. For the prominent A_g mode, the full width at half maxima (FWHM) of ammonium molybdate-derived samples is 58 cm^{-1}, whereas for sodium molybdate-derived sample it is 15 cm^{-1}. At lower temperatures, peaks are also observed at 282 and 357 cm^{-1}, associated with the B_{2g} vibrational mode of the 2H phase, indicating a mixed 1T and 2H phases. At higher temperature, NHMo-2 existed in the 1T phase only, which was confirmed by the absence of the B_2g mode. The assigned Raman modes with FWHM and intensity are summarized in Table 5. Thus, ammonium molybdate first gives rise to multi-phase growth of $MoTe_2$ that tends towards 1T dominance when heated, whereas sodium molybdate prefers the formation of crystalline 1T phase.

Table 4 — The crystallite sizes and strains of different samples.

Sample	Crystallite size (Scherrer's equation) (nm)	Crystallite Size (W-H plot) (nm)	Strain from the W-H plot
NAMo-1	56	144	1.8×10^{-3}
NAMo-2	45	91	1.4×10^{-3}
NHMo-1	28	56	2.6×10^{-3}
NHMo-2	45	41	8.2×10^{-4}

Table 5 — Different Raman modes along with FWHM and Raman shift.

Sample name	RAMAN Mode	FWHM (cm^{-1})	Raman Shift (cm^{-1})
NAMo-1	^1A_g	15	117
	^2A_g	12	138
NAMo-2	^1A_g	17	117
	^2A_g	15	138
NHMo-1	^1A_g	58	120
	^2A_g	16	139
	B_{2g}	25	287
NHMo-2	^1A_g	17	120
	^2A_g	15	139
	B_{2g}	22	201

3.5 Fourier transform infrared spectroscopy (FT-IR)

FT-IR spectroscopy was employed to analyze the molecular structure and chemical bonding of the synthesized $MoTe_2$. In Fig. 6(a), the sample NAMo-1 exhibits a clear absorption peak at 603, 867, 928 and 1413 cm^{-1}, corresponding mainly to Mo-Te, Mo-O metal bonding, and O-H bond vibrations, respectively. These peaks demonstrate efficient incorporation of metal-chalcogen bonds [24,31]. When the temperature increases, the developed sample (NAMo-2) exhibits Mo–Te vibrational modes at 614 and 934 cm^{-1}, whereas the O-H vibrations shift to 1402 cm^{-1} from 1413 cm^{-1}. In Fig. 6(b), sample NHMo-1 shows the Mo–Te stretching modes at 584 cm^{-1} and the Mo-O bond at 861 and 925 cm^{-1} [32]. As the temperature increases, these modes are observed at 455, 841 and 923 cm^{-1}. A detailed assignment of vibrational modes corresponding to functional groups is summarized in Table 6. Thus, the FTIR spectra confirms the presence of Mo-Te bond vibrations in all samples regardless of the precursor.

3.6 Possible growth mechanism

The morphological, structural and spectroscopic analysis of $MoTe_2$ nanostructures described the growth

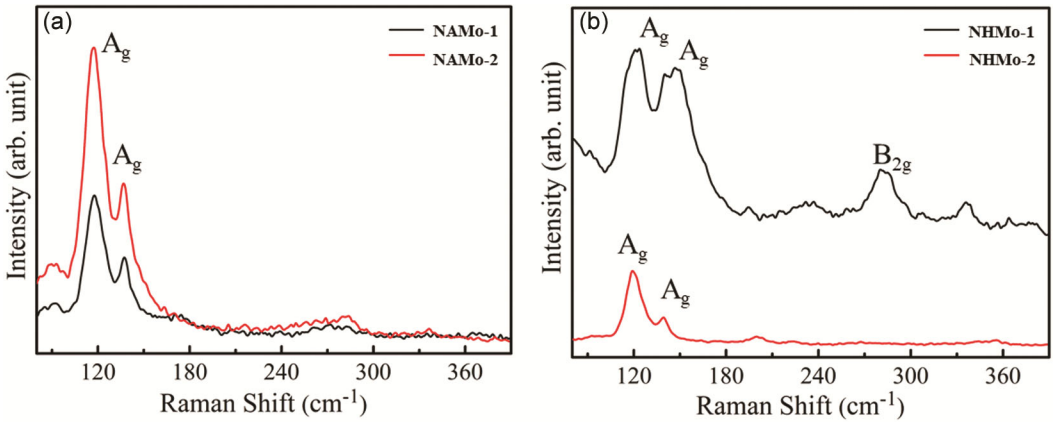


Fig. 5 — Raman spectra of (a) NAMo-1 & NAMo-2 and (b) NHMo-1 & NHMo-2, of $MoTe_2$ structures.

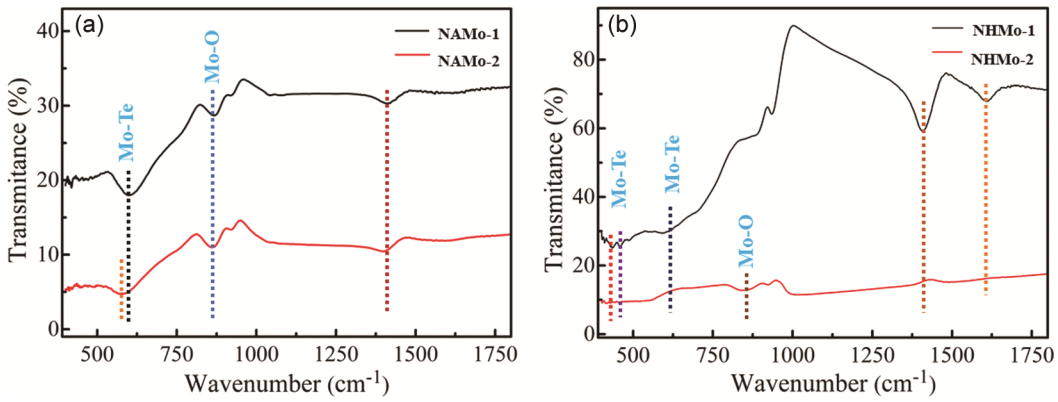


Fig. 6 — FT-IR spectra of (a) NAMo-1 & NAMo-2 and (b) NHMo-1 & NHMo-2, of $MoTe_2$ structures.

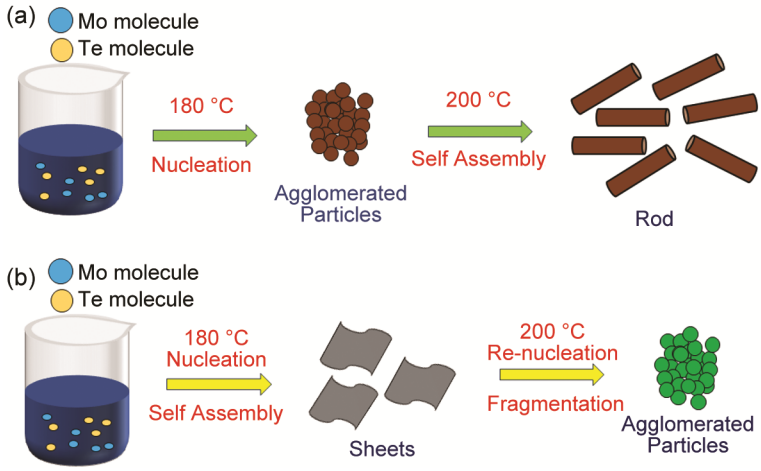


Fig. 7 —Schematic diagram of growth process of $MoTe_2$ using (a) sodium molybdate and ammonium molybdate, and (b) as Mo precursor.

Table 6 — Vibrational modes and their assignments.

Wave number (cm^{-1})	Vibrational bond
455, 584, 614	Mo-Te[24,31]
834, 867, 928	Mo-O[24]
1401	O-H[24]

mechanism depending on the precursors used and temperature. A schematic diagram of the growth process for the synthesized samples is shown in Fig. 7(a, b). The chemical reaction involved in the synthesis process is described, by Eq. 3-8:

Firstly, Te and $NaBH_4$ react and form NaHTe. $NaBH_4$ is used as a reducing agent[33,34]

$$NaBH_4 + Te + 3H_2O \rightarrow NaHTe + B(OH)_3 + 3H_2 \quad \ldots (3)$$

and sodium molybdate is reduced to MoO_4^{2-} when it reacts with DI[12],

$$Na_2MoO_4.2H_2O + H_2O \rightarrow 2Na^+ + MoO_4^{2-} + 3H_2O \quad \ldots (4)$$

NaHTe reacts with MoO_4^{2-} and formed the $MoTe_2$

$$Mo^{4+} + 2Te^{2-} \rightarrow MoTe_2 \quad \ldots (5)$$

while ammonium molybdate is reduced to MoO_4^{2-} when it reacts with DI [23]

$$(NH_4)_6\,MoO_7O_{24}.2H_2O + H_2O \rightarrow Mo_7O_{24}^{6-} + 6NH_4^+ + 3H_2O \quad \ldots (6)$$

$$Mo_7O_{24}^{6-} + 4H_2O \rightarrow 7MoO_4^{2-} + 8H^+ \quad \ldots (7)$$

NaHTe reacts with MoO_4^{2-} and formed $MoTe_2$

$$Mo^{4+} + 2Te^{2-} \rightarrow MoTe_2 \quad \ldots . (8)$$

The choice between sodium molybdate (Na_2MoO_4) and ammonium heptamolybdate [$(NH_4)_6Mo_7O_{24}$] significantly affects the nucleation kinetics and morphology through differences in solution speciation and Mo^{6+} availability. Sodium molybdate dissolves to

form monomeric $[MoO_4]^{2-}$ tetrahydrate in alkaline solution, where $NaBH_4$ reduces both the molybdate species and activates Te surfaces [12], promoting rapid nucleation of $MoTe_2$ into nanorods, as shown in Fig. 1 (c, d) [12]. The formation of $MoTe_2$ was verified by the XRD peaks, Raman bands and lattice-resolved HRTEM images. In contrast, ammonium heptamolybdate provides polyoxo-Mo clusters $[Mo_7O_{24}]^{6-}$, where $NaBH_4$ slowly reduces polyoxo-Mo to Mo^{4+}, hence favors nucleation of $MoTe_2$ into nanosheet/flakes like structures [35,36]. This suggests that Na_2MoO_4 adopts a temperature-controlled pathway through random agglomerates to rods, whereas $(NH_4)_2Mo_7O_{24}$ experiences an ammonium-assisted transformation from stacked nanosheets/flakes at lower temperature to broken particles at high temperature.

4 Conclusion

Here, $MoTe_2$ nanostructures were developed using two different precursors and at two different temperatures via hydrothermal methods. Sodium molybdate precursor promotes the development of monoclinic 1T-$MoTe_2$, transitioning from nano-clustered particles at lower temperature to well-defined nanorods at higher temperature. On the other hand, ammonium molybdate prefers the formation of mixed phase $MoTe_2$, stacked nanosheets/flakes at lower temperatures, which break into nanoparticles at higher temperature. The average crystallite size, calculated using the W-H plot is 144, 91, 57, and 41 nm for NAMo-1, NAMo-2, NHMo-1 and NHMo-2, respectively. The active A_g and B_{2g} modes were confirmed by Raman spectra and characteristic Mo-Te and Mo-O vibration modes were observed in Fourier-transform infrared spectra, further confirmed the formation of $MoTe_2$ nanostructures. These findings establish a foundation for controlling the morphologies of $MoTe_2$ for specific applications in electronics, catalysis, and energy conversion.

References

1 Shinde P V, Hussain M, Moretti E & Vomiero A, *Sus Mat*, 4 (2024) 236.
2 Radomski P & Szary M J, *Acta Mater*, 272 (2024) 119949.
3 Jones L A H, Xing Z, Swallow J E N, Shiel H, Featherstone T J & Smiles M J, *J Phy Chem C*, 126 (2022) 21022.
4 Aneesha & Mehata M S, *Mater Res Bull*, 185 (2025) 113287.
5 Bhatt N & Mehata M S, *Mater Res Bull*, 192 (2025) 113633.
6 Phalswal P, Khanna P K, Rubahn H G & Mishra Y K, *Mater Adv,* 3 (2022) 5672.
7 Geng X, Zhang Y, Han Y, Li J, Yang L & Benamara M, *Nano Lett*, 17 (2017)1825.
8 Park J C, Yun S J, Kim H, Park J H, Chae S H & An S J, *ACS Nano*, 9 (2015) 6548.
9 Ding L, Wei J, Qiu Y, Wang Y, Wen Z & Qian J, *Chem Eng J*, 407 (2021) 127213.
10 Vikraman D, Hussain S, Rabani I, Feroze A, Ali M & Seo Y S, *Nano Energy*, 87 (2021) 106161.
11 Karki H P, Kim H, Jung J & Oh J, *Nano mater*, 11 (2021) 2346.
12 Li H Y, Yao C B, Shi B Y, Cao H X, Zheng X Y & Liu Y, *J Alloys Compd*, 939 (2023) 168697.
13 Lei Y, Xiao X, Ma T, Li W, Zhang H, & Ma C, *Front Chem*, 10 (2022) 1005782.
14 Wang F, Li G, Zheng J, Ma J, Yang C & Wang Q, *RSC Adv*, 8(2018) 38945.
15 Nagaraju G, Tharamani CN, Chandrappa GT, & Livage J, *Nanoscale R Lett*, 2 (2007) 461.
16 Sharma P, Singh M K & Mehata M S, *J Mol Struct*, 1249 (2022) 131651.
17 Mehata M S, Singh M K, Awasthi K, Sharma P, Rana S & Ohta N, *J Phy Chem C*, 125(2021) 26566.
18 Karfa P, Majhi K C & Madhuri R, *Int J Hydrogen Energy*, 44 (2019) 24628.
19 Wan Q, Li M, Zhou Y, Zhang M, Xu Z & Wang J, *Comm Mater,* 6 (2025) 18.
20 Meena A, Saleem H, Shanmugam N, Kumar A S, Suthakaran S & Ayyar M, *J Mater Sci: Mater in Electr*, 36 (2025) 613.
21 Zhang Z, Wang J, Li Y, Zhang S, Xiao L & Wang J, *Int J Hydrogen Energy*, 48 (2023) 4207–19.
22 Yu B, Huang A, Srinivas K, Zhang X, Ma F & Wang X, *ACS Nano*, 15 (2021) 13279.
23 Bai J, Zhang L, Li S, Ren H, Liu Y & Guo S, *Chem Eng J*, 452 (2023) 139111.
24 Shinde P V, Mane P, Late D J, Chakraborty B & Rout C S, *ACS Appl Energy Mater*, 4 (2021) 11886.
25 Bhat K S & Nagaraja H S, *Int J Hydrogen Energy*, 44 (2019) 17878.
26 Liu M, Wang Z, Liu J, Wei G, Du J & Li Y, *J Mater Chem A Mater*, 5 (2017) 1035.
27 Xu T, Li A, Wang S, Tan Y & Cheng X, *Nano mater*, 12 (2022) 4133.
28 Manh D H, Ngoc Nha T T, Hong Phong L T, Nam P H, Thanh T D & Phong P T, *RSC Adv,* 13 (2023) 25007.
29 Jabir S A A & Harbbi K H, *AIP Conf Proc*, (2020) 2307.
30 Fraser J P, Postnikov P, Miliutina E, Kolska Z, Valiev R & Svorcik V, *ACS Appl Mater Interf*, 12 (2020) 47774.
31 Vojtekova T, Slusna LP, Dobrocka E, Precner M, Sojkova M & Hrda J, *Phys Status Solidi B Basic Res,* 260 (2023) 2300250.
32 Berwal P, Rani S, Sihag S, Singh P, Dahiya R & Kumar A, *Inorg Chem Commun*, 159 (2024) 111833.
33 Jiang X, Wang J & Zhou B, *Diam Relat Mater*, 130 (2022) 109437.
34 Zhang K, Suh J M, Choi J W, Jang H W, Shokouhimehr M & Varma R S, *ACS Omega*, 4 (2019) 483.
35 Bansode S R, Harpale K, Khare R T, Walke P S & More M A, *Mater Res Express*, 3 (2016) 115023.
36 Li M, Wang D, Li J, Pan Z, Ma H & Jiang Y, *RSC Adv*, 6 (2016) 71534.